

# Detecting Vortex Formation and Shedding in Cylinder Wakes using Lagrangian Coherent Structures

Matthew P. Rockwood\*

Kunihiko Taira<sup>†</sup>

*Syracuse University, Syracuse, NY, 13244*

*Florida State University, Tallahassee, Florida 32310*

Melissa A. Green<sup>‡</sup>

*Syracuse University, Syracuse, NY, 13244*

The wake behind a circular cylinder is studied to investigate the complex vortex shedding physics in the near-wake region. Both the  $Q$  criterion and a Lagrangian coherent structure (LCS) analysis are applied to flow fields acquired from a numerical simulation as well as from experimental particle image velocimetry (PIV) to determine the properties of the wake. A rate-of-strain filter is applied to the finite-time Lyapunov exponent (FTLE) field to filter out ridges corresponding to local shear, and yields ridges along which fluid trajectories separate hyperbolically. This strain filter reveals a sudden loss of hyperbolicity along an LCS as a new vortex begins to form. The LCS are also shown to identify and track topological Lagrangian saddle points in the cylinder near wake. This information characterizes the behavior of the vortices as they form, shed, and convect downstream. In particular, a Lagrangian saddle point is observed to remain attached to the cylinder surface until the vortex separates and then consequently accelerates downstream with a similar track in both numerical and experimental results. The present approach provides a novel criterion for the identification of vortex shedding.

## Nomenclature

$Re$  Reynolds Number

$\nabla$  Gradient function

$\mathbf{u}$  Velocity vector

---

\*Ph.D. Student, Mechanical and Aerospace Engineering Department, Syracuse University, AIAA Student Member.

<sup>†</sup>Assistant Professor, Mechanical Engineering Department, Florida State University, AIAA Senior Member.

<sup>‡</sup>Assistant Professor, Mechanical and Aerospace Engineering Department, Syracuse University, AIAA Senior Member.

$\mathbf{S}$	Rate of strain tensor
$\mathbf{\Omega}$	Rate of rotation tensor
$\mathbf{x}$	Location vector
$T$	Shedding period
$\tau$	Integration time
$\sigma_\tau$	Coefficient of expansion
$\lambda_{max}$	Maximum matrix eigenvalue
$\mathbf{n}$	Normal vector
$D$	Cylinder diameter

## I. Introduction

The wake behind a circular cylinder is a canonical flow that has implications in the control of vortex shedding from a variety of bluff bodies. At low Reynolds numbers based on cylinder diameter ( $Re > 47$ ) an unsteady wake develops behind the circular cylinder due to instabilities in the separation bubble that result in periodic shedding of vortices in a 2S pattern, or von Kármán vortex street.<sup>1</sup> This vortex shedding results in oscillating fluid forces being experienced by the cylinder that lead to the risk of problems related to structural fatigue.<sup>2,3</sup>

At Reynolds numbers below the critical value of 47, a steady separation bubble forms in the wake of the cylinder. As the Reynolds number increases beyond 47, the transition to the unsteady wake occurs. The physical mechanism that brings about this change has been analyzed and discussed thoroughly in previous studies. The formation of a vortex behind the cylinder at Reynolds numbers below 350 is attributed to the presence of high shear near the base of the cylinder along with the induced velocity field caused by the momentum deficit.<sup>4</sup> As the vortex grows, its induced velocity begins to pull fluid from the opposite shear layer towards the vortex core.<sup>5</sup> Since this fluid is from the opposite shear layer, it has opposite vorticity and causes the vortex to push away from the cylinder. Once it begins to move downstream, it no longer has access to the strong shear that formed it, so the vortex strength no longer increases. Inside the separation bubble, vortex sheets undergo multiple folds that eventually lead to the vortex roll-up.<sup>6</sup> It was later found that an absolute instability in the near wake creates a self-sustaining motion of fluid just behind the cylinder that allows the fluid to enter the separation bubble in an alternating periodic manner.<sup>7</sup> This absolute instability determines the shedding frequency of the vortices by controlling the rate at which the fluid enters the separation bubble. The interaction between the two sides of the cylinder wake was further studied by placing a small “control” cylinder in the shear layer on one side of the wake.<sup>8</sup> When the small cylinder was placed correctly at Reynolds numbers below 100 the shear layer interactions were inhibited in the wake just

downstream of the main cylinder, and the vortex shedding was effectively eliminated. Similarly, a numerical study of a constricted channel flow proposed that a wave instability leads to the amplification of the pressure gradient leading to vortex splitting, and eventually vortex shedding.<sup>9</sup>

In the past couple of decades, an increasing number of studies have been focused on stability analysis of the cylinder wake. A low-dimensional dynamical system approach using an incompressible potential flow model of the cylinder wake<sup>10</sup> found that vorticity perturbations introduced anywhere on the symmetry line in a steady wake ( $Re < 48$ ) decayed, but vorticity perturbations introduced on the symmetry line outside of the separation bubble grew and caused the transition to the unsteady vortex street if the Reynolds number was above 48. A numerical study that looked for the mechanism that sustains the wake oscillation at Reynolds number above the critical value found that any small, localized disturbance propagated both up and downstream. When the disturbance reached the cylinder, it caused oscillation in the separation bubble leading to the global instability.<sup>11</sup> The receptivity of the cylinder wake was also examined in detail with structural stability analysis.<sup>12</sup> Stability analyses such as these are useful for determining the mechanism that dominates the unsteady shedding.

Many research groups have recently explored controlling the shedding off a circular cylinder with active or passive flow control techniques. The use of synthetic jets<sup>13</sup> at Reynolds numbers of 500 and 3900 both showed a reduction in drag coefficient by approximately 12%. Low power electrohydrodynamic actuators were shown to have a significant effect on the qualitative structure of the wake at  $Re = 2500$ , but at Reynolds numbers of the order of 50,000 they had a small effect on the time-averaged separation location.<sup>14</sup> By attaching longitudinally oriented o-rings to the cylinder,<sup>15</sup> a drag reduction of 9% was realized at  $Re = 120,000$ . This drag reduction was thought to be due to the elongation of the vortex formation region. The addition of v-cut microgrooves to the cylinder surface<sup>16</sup> created a 7.6% drag reduction at  $Re = 3600$ , but a 4.2% drag increase at  $Re = 36,000$ . Dielectric barrier discharge plasma actuators were used to demonstrate a drag reduction of 32% at  $Re = 15,000$ , but required 50 times more power than was conserved from drag reduction.<sup>17</sup> A combination of suction and blowing was numerically shown<sup>18</sup> to effectively eliminate the oscillatory forces on the cylinder at Reynolds numbers up to 1000. While several techniques at low Reynolds numbers have shown adequate control of vortex shedding, the techniques require a significant amount of power, lose their effectiveness, or cost too much to implement in most practical applications at  $Re = O(10^5 - 10^9)$ . The goal of the current research is to obtain a different representation of the flow that could lead to the development of a system that adequately controls the unsteady shedding at a reasonable power requirement for a range of parameters.

Previous attempts to determine the coherent vortex structures in the wake primarily used Eulerian techniques, which are based on the instantaneous velocity field and its gradient.<sup>19,20</sup> The term coherent

structures was first used by Brown and Roshko<sup>21</sup> to describe regions in a turbulent mixing layer that exhibited coherence over a reasonable length of time. In our current work, the vortices shed from a circular cylinder are the coherent structures present so the terms are used interchangeably. In this paper, the Eulerian  $Q$  criterion<sup>22</sup> is compared with the finite-time Lyapunov exponent (FTLE) field,<sup>23</sup> a Lagrangian quantity that is calculated using integrated particle trajectories, and from which we extract Lagrangian coherent structures (LCS). An LCS analysis uncovers the transport boundaries where particles separate hyperbolically in the flow, and the analysis presented here includes a rate-of-strain filter to eliminate regions of high shear from the LCS identification process.<sup>24</sup> Some applications of LCS analysis include the study of unsteady wakes behind a pitching panel,<sup>25</sup> non-axisymmetric vortex rings,<sup>26</sup> oceanic eddies,<sup>27</sup> **cardiovascular flows**,<sup>28</sup> fluid transport of translating and flapping wings,<sup>29</sup> and hurricanes.<sup>30</sup> An extensive review of LCS was written by Haller.<sup>31</sup> Combined with a closed-loop control scheme, inclusion of an LCS analysis in a combustion flow control application increased mixing in simulated flow around a square cylinder.<sup>32</sup> In that work, wall-tangential velocity sensors were correlated with the characteristics and behavior of the local LCS, and wall-tangential velocity actuators were driven to increase the LCS interaction in the downstream wake. The current study is attempting to gain the understanding of a canonical bluff body shedding flow that would be necessary to apply similar strategies to alter the dynamics of shedding.

In general, an LCS analysis yields co-dimension one structures in a flow field. These structures correspond to lines and surfaces in two and three-dimensional flows, respectively. By implementing the analyses in specific ways, both attracting and repelling manifolds are obtained. The work presented in this paper primarily focuses on the behavior of topological Lagrangian saddle points, identified as intersections of these attracting and repelling lines in the two-dimensional cylinder wake. The current study analyzes the dynamics of vortex-bounding Lagrangian saddle points using data from both a numerical simulation and experiments. While the two data sets are not matched in Reynolds number, the saddle point dynamics are the same in both cases. Lagrangian saddle point dynamics have also been shown to be present and important in three-dimensional turbulent flows, and the emergence of saddles was shown to accompany the birth of secondary hairpin vortices in a turbulent channel DNS.<sup>33</sup> LCS saddles have been used to develop generalized vortex tracking techniques, and vortex wake breakdown has been observed to accompany the merging of two independent saddles in an LCS analysis of PIV data in the wake of a bio-inspired pitching panel or airfoil.<sup>25,34,35</sup> The work presented here demonstrates the potential for robust methods of tracking LCS saddle points to identify the formation and shedding of coherent structures in general bluff body flows, as opposed to the standard Eulerian analyses that may suffer from the velocity field noise that is common with experimentally-acquired data.

## II. Method

### A. Eulerian $Q$ Criterion

The Eulerian criterion employed in the present study is the  $Q$  criterion proposed by Hunt et al.<sup>22</sup> Several other criteria have been used in similar analyses previously ( $\Delta$ ,<sup>36</sup>  $\lambda_2$ ,<sup>37</sup>  $\Gamma_1$ <sup>38</sup>), but do not yield distinctly dissimilar results, and  $Q$  is chosen for presentation here for simplicity and for consistency with other similar studies in the literature. The velocity gradient tensor can be decomposed into the symmetric rate of strain tensor,  $\mathbf{S}$ , and the anti-symmetric rate of rotation tensor,  $\mathbf{\Omega}$ :

$$\nabla\mathbf{u} = \mathbf{S} + \mathbf{\Omega}, \quad (1)$$

where  $\mathbf{S} = \frac{1}{2}[\nabla\mathbf{u} + (\nabla\mathbf{u})^T]$  and  $\mathbf{\Omega} = \frac{1}{2}[\nabla\mathbf{u} - (\nabla\mathbf{u})^T]$ . The  $Q$  value is defined as the relative difference between the magnitude of the rate of rotation and strain tensors (and is the second invariant of the rate of deformation tensor):

$$Q = \frac{1}{2}[\|\mathbf{\Omega}\|^2 - \|\mathbf{S}\|^2], \quad (2)$$

where  $\|\mathbf{\Omega}\|$  represents the Euclidean (Frobenius) norm of  $\mathbf{\Omega}$ . Locations in the flow with positive  $Q$  values are defined as vortices using this criterion, as they contain local rotational motion.

While the  $Q$  criterion is Galilean invariant, or unaffected by translations of the frame of reference, it can lead to misrepresentation of vortices when there are rotating or accelerating frames of reference. While this is not the case in the current example, it does affect the broader applicability of any derived identification and tracking schemes. This criterion can find vortex cores effectively in non-accelerating frames, but even then a subjective threshold such as a percentage of the maximum value across all times is often defined as the boundary of the vortex in practical implementation. This is especially true in noisier experimental data sets and three-dimensional flows.

### B. Lagrangian Coherent Structure Analysis

LCS analysis was initially introduced to the fluid mechanics community by Haller,<sup>23</sup> which extracted Lagrangian coherent structures from the finite-time Lyapunov exponent (FTLE) field. The ridges of high FTLE indicate candidate material lines in the flow where particle trajectories diverge in time. The ridges have been used effectively to mark the transport boundaries in a given flow field. This is in contrast to more recent work that locates elliptic LCS, which can be described as the boundaries of coherent sets of fluid that make up vortices.<sup>39</sup> For this work, the analysis code that was originally developed by Green et al.<sup>24</sup> was used to generate the FTLE fields from which the LCS are extracted. In order to calculate an FTLE field,

particle tracers must be tracked for a finite amount of time, for which velocity data for the spatial domain and temporal range of interest must be available. At a given instant of time ( $t_0$ ), a fine grid of particle trajectories is initialized in the domain ( $\mathbf{x}_0$ ) and are advected forward in time using a fourth-order Runge–Kutta integrator. With  $\mathbf{x}(\mathbf{x}_0, t_0, \tau)$  defined as the fluid trajectory locations at time  $\tau$  that were initialized at  $(\mathbf{x}_0, t_0)$ , the FTLE value is defined on  $\mathbf{x}_0$  as:

$$FTLE_\tau(\mathbf{x}_0, t_0) = \frac{1}{2\tau} \log \sigma_\tau(\mathbf{x}_0, t_0), \quad (3)$$

where the coefficient of expansion,  $\sigma_\tau$ , is the largest eigenvalue of the Cauchy–Green strain tensor defined as:

$$\sigma_\tau(\mathbf{x}_0, t_0) = \lambda_{max} \left( \left[ \frac{\partial \mathbf{x}(t_0 + \tau, \mathbf{x}_0, t_0)}{\partial \mathbf{x}_0} \right]^* \left[ \frac{\partial \mathbf{x}(t_0 + \tau, \mathbf{x}_0, t_0)}{\partial \mathbf{x}_0} \right] \right). \quad (4)$$

Here, \* indicates the matrix transpose.

At each point in space, FTLE is a scalar measure of the maximum rate of separation over an integration time  $\tau$  between two particles that were initially separated by a finitely small distance near that point. If a group of particles travel together, for example in a uniform flow, the local FTLE value is very small. If the two particles are on either side of a hyperbolic LCS, their trajectories will hyperbolically repel over time, causing the local FTLE value to be high. The FTLE scalar field is calculated on the grid of initial trajectory points, and the regions of large-magnitude positive FTLE create maximizing ridges. We define these maximizing ridges as Lagrangian coherent structures, and they are extracted using a fixed threshold of the FTLE values. It is important to note that changing the threshold value for FTLE ridge extraction does not change the location or shape of the coherent structures identified, only the thickness of the ridges.

The FTLE calculation initialized at time  $t_0$  can also be performed by advecting fluid trajectories in negative time. Regions of large magnitude negative-time FTLE will indicate ridges that are attracting flow at time  $t_0$ , as fluid trajectories that stretch apart when integrated in negative time are attracted to a local region when advected in positive time. Therefore, if the values are integrated in both positive and negative (forward and backward) time, both repelling FTLE ridges (pLCS) and attracting FTLE ridges (nLCS) at initial time  $t_0$  can be extracted using the maximum eigenvalues of the two different Cauchy–Green strain tensors. For both positive- and negative-FTLE, the scalar fields are defined at  $t_0$ , and those scalar fields indicate the current flow attraction and repulsion, and are therefore representative of the current flow topology. To calculate the FTLE fields at a later time, for example at the next phase of velocity data  $t_1$ , a new grid of trajectories initialized at  $t_1$  are calculated. Others have used the composition of trajectory information,<sup>40</sup> have advected LCS ridges,<sup>41</sup> and have used both the maximum and minimum eigenvalues of the Cauchy–Green strain tensor<sup>42</sup> to enable an increase in the efficiency of computing many FTLE fields in

a certain time range. These attracting and repelling ridges in the flow are used to outline the flow structures by showing the transport boundaries between distinct vortices and the free stream. As the  $Q$  criterion only visualizes the vortex cores, the ability to identify the transport boundaries objectively provides additional insight into the vortex dynamics, especially when studying the interactions among coherent structures.

The FTLE has been demonstrated to be robust to velocity field errors that are small in magnitude or short in duration.<sup>43</sup> Having poor spatial or temporal resolution can have a negative effect on the exact LCS location in some cases, but the mean location of the LCS is not affected.<sup>44</sup> In the present study, we apply a rate-of-strain filter on the FTLE ridges to ensure that only those with hyperbolically attracting or repelling behavior, as is expected at coherent structure boundaries, are captured and not those that indicate shear strain.<sup>43,45</sup> The filter was applied to each time set of LCS independently and is defined using the inner product of the rate of strain and the LCS normal vector as:

$$\langle \mathbf{n}(t_0, \mathbf{x}_0), \mathbf{S}(t_0, \mathbf{x}_0)\mathbf{n}(t_0, \mathbf{x}_0) \rangle \geq 0, \quad (5)$$

where  $\langle \cdot, \cdot \rangle$  is the vector inner product and  $\mathbf{n}(t_0, \mathbf{x}_0)$  is the normal vector to the LCS. LCS are considered hyperbolically attracting or repelling if this filter is positive for pFTLE ridges or negative for nFTLE ridges.

The normal vector was calculated as the eigenvector associated with the maximum eigenvalue of the Hessian matrix of the scalar FTLE field. This corresponds to the direction of maximum curvature. Using the eigenvector of the Hessian is a noisy technique that can result in errors in the rate-of-strain calculation. This is visible in later figures by the speckled appearance along some portions of the LCS after the rate-of-strain filter is applied. An example of the normal vectors used is shown in figure 1(a), and the negative gradient of FTLE is shown for reference in figure 1(b). The gradient works well in the majority of the flow, but fails to find the normal vector when the points fall very close to the peaks of the FTLE ridge. Since we are specifically interested in the results close to the FTLE ridges, the gradient technique is not used. The eigenvector of the Hessian better captures the normal vectors in the near-ridge region, but occasionally has large errors, for example in the region near  $(x, y) = (0.65, 0.55)$ . It is worth noting that the normal vectors are not required to be outward normal, as we are evaluating an inner project of  $\mathbf{n}$  with itself, weighted by  $\mathbf{S}$  in equation 5. In general, the eigenvector of the Hessian performs well enough to accentuate the difference between a hyperbolic LCS or a shear LCS.

While determining the FTLE field requires a Lagrangian calculation, each FTLE field represents the current topology. Therefore, by applying the rate-of-strain filter to the FTLE ridges at the time they are valid, it ensures that the FTLE ridges are exhibiting hyperbolic repulsion (along pLCS), or hyperbolic attraction (along nLCS). This technique was applied instead of the uniformly hyperbolic criterion that has been applied by Olascoaga and Haller<sup>46</sup> that further restricts LCS by requiring they be hyperbolic for the

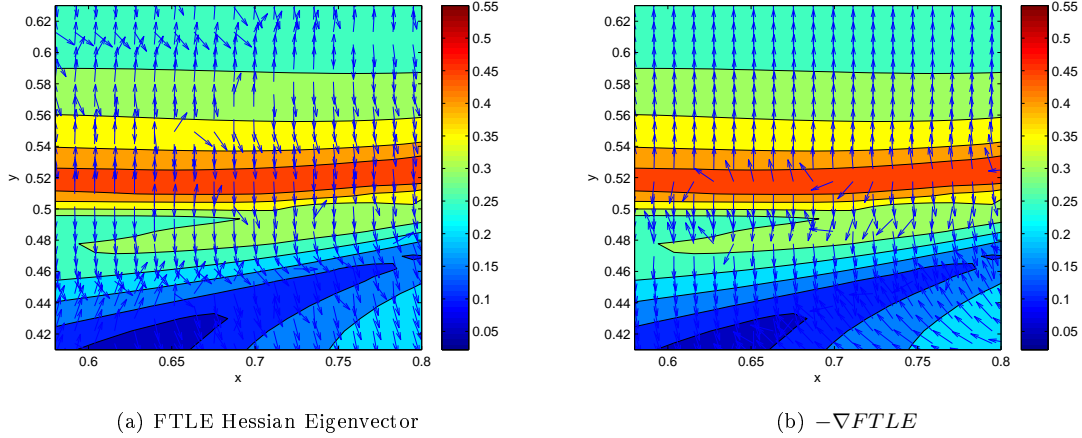


**Figure 1.** Contours of FTLE with a superimposed quiver plot showing the computed LCS normal vectors based on the (a) eigenvector of the largest eigenvalue of the FTLE Hessian and (b) negative gradient of FTLE.

full integration time. Instantaneous loss of hyperbolicity has been shown to correspond to the formation of a new vortex in the flow,<sup>24</sup> and therefore information related to the start of vortex formation near the cylinder surface would be lost if the uniformly hyperbolic criterion was applied.

### C. Numerical Simulation

The simulation data used in the LCS analysis was generated with the immersed boundary projection method.<sup>47, 48</sup> Two-dimensional incompressible flow was simulated with the projection-based solver on a Cartesian grid on which the immersed boundary technique was utilized to create a circular cylinder. The boundary force was treated as a Lagrange multiplier and was determined fully implicitly using a null-space and fast Fourier transform method. The approach enforces the no-slip boundary condition along the cylinder surface through a single projection. The immersed boundary method used in the present study achieves accuracy order of 2 and 1.5 in time and space, respectively.

The immersed boundary projection method was validated for a wide variety of flow problems including the steady and unsteady viscous flow over a circular cylinder.<sup>48, 49</sup> Extensive discussions on the verification and validation were provided by Colonius and Taira<sup>48</sup> and Munday and Taira.<sup>49</sup> The current research used 120 velocity field snapshots per shedding period generated from the numerical simulation at a Reynolds number  $Re = U_\infty D/\nu = 100$ , where  $U_\infty$ ,  $D$  and  $\nu$  are the freestream velocity, cylinder diameter, and kinematic viscosity of the fluid, respectively. FTLE was calculated using an integration time of two shedding periods ( $\tau = 2T$ ), and was selected to yield well defined FTLE ridges. As long as the integration time was long enough to allow the tracked particles to sufficiently separate ( $\tau \geq 0.5T$ ), changes in the integration time had a negligible effect on the location of the FTLE ridges in the flow field, consistent with Kourentis and

Konstantinidis,<sup>50</sup> and Bourgeois et al.<sup>51</sup>

The computational domain was discretized with multiple levels of grid refinement by having five nested grids. The overall size of the computational domain was set to  $(x/D, y/D) \in [-31, 33] \times [-32, 32]$ . Along the far-field boundary, uniform flow was specified and the spatial setup has been verified to ensure that the near-field solution was not affected. For the considered Reynolds number, grid size of  $\Delta x/D = 0.02$  was used in the vicinity of the cylinder. The time step was selected so that the CFL number based on the finest spatial grid and the maximum velocity throughout the simulation was less than 0.5.

#### D. Experimental Setup

Particle image velocimetry (PIV) experiments were conducted in a water tunnel with a  $0.6 \text{ m} \times 0.6 \text{ m} \times 2.4 \text{ m}$  test section. A cylinder diameter of 60 mm was used, at a free stream speed of 150 mm/s, which resulted in an experimental Reynolds number of 9000. The observed von Kármán vortex shedding frequency was 0.53 Hz, which corresponded to a Strouhal number of 0.21 using the cylinder diameter as the wake width. Dantec polyamid particles with a diameter of 20  $\mu\text{m}$  were used to seed the flow, and a Gemini Nd-Yag 200-15 laser was used to illuminate the flow in a single spanwise-constant plane. Two 1.3 megapixel HiSense PIV cameras were used to capture the images at a rate of 4.0 Hz. Each camera had a measurement window of  $1280 \times 1024 \text{ px}$  with a spatial resolution of 4.8 px/mm, which provided a field of view of approximately  $267 \times 213 \text{ mm}$ . An interrogation window size of  $16 \times 16 \text{ px}$  was used with an overlap of 50%. This yielded a grid spacing of 8 px or 1.7 mm which is about  $0.03D$ . 3000 image pairs were captured by the two cameras simultaneously, and the resulting instantaneous velocity vector fields were stitched together by bilinearly interpolating onto a common grid encompassing both domains. The cameras were then moved to a location further downstream to increase the total field of view, and the process was repeated. The stitched velocity fields at each downstream location were phase-averaged into 18 phases per period using the static pressure signal collected at 70 degrees from the upstream stagnation point to increase the temporal resolution of the data for the Lagrangian calculations. The phase-averaged results were then stitched together which resulted in a full field of view of  $590 \times 193 \text{ mm}$ . The pressure tap location was chosen to ensure the signal was dominated by the von Kármán vortices, and therefore was located upstream of the separation point.<sup>52</sup> The static pressure was collected using an Omega PX409 wet-dry differential pressure transducer and a National Instruments PXIe DAQ system. While the experimental cylinder flow at  $Re = 9000$  is three dimensional, recent work has shown that planar FTLE calculations are not affected by the three-dimensionality of the flow when the vortex is nearly perpendicular to the PIV plane.<sup>53</sup>

Due to limitations in tunnel speed and cylinder diameter, Reynolds number matching between the available simulation results and the experiments was not possible. The results are qualitatively similar as the

fundamental processes dominating the vortex shedding are not expected to change over this range of Reynolds numbers.

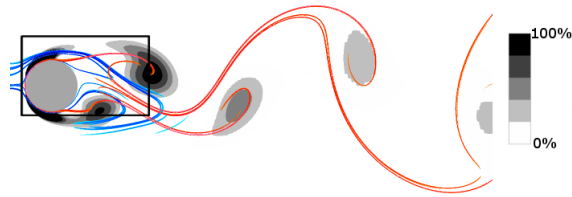


**Figure 2.** nLCS (red), pLCS (blue), and  $Q$  criterion (grey contours, % of global maximum) for  $Re = 100$ .

### III. Results

For the purposes of this paper, FTLE and  $Q$  criterion were calculated at twelve instants of time that span one period of fully-developed vortex shedding in the numerical data. Figure 2 is an example of the full numerical LCS at the first phase before the rate-of-strain filter is applied. The colorbar displayed is for the  $Q$  criterion, and is the same for all subsequent figures representing the simulation data. All images display the LCS as FTLE values greater than 67% of the maximum FTLE value. An integration time of two shedding periods was used for all FTLE calculations with an integration time step of  $0.005T$  in the numerical calculation and  $0.06T$  in the experimental calculation. The box in figure 2 displays the region that will be analyzed subsequently in more detail. In each of the figures the nLCS (attracting material lines) are shown in red, the pLCS (repelling material lines) are shown in blue, and the contours of  $Q$  (vortex cores) are shown in shades of grey, with darker grey indicating higher  $Q$  magnitude. All regions with positive  $Q$  are included, and were scaled to clearly display regions with even low magnitude  $Q$  values. This allows us to observe the earliest possible Eulerian vortex formation process behind the cylinder.

As seen in figure 2, the LCS successfully outline the transport boundaries at the edges of the vortices in the cylinder wake. The  $Q$  criterion and the LCS are in agreement on the locations of the shed vortices, with the LCS clearly wrapping around the vortex cores highlighted by the  $Q$  criterion. By using the LCS to more closely analyze the flow just behind the cylinder, we gain insight into the shedding process.

#### A. Identification of Vortex Formation via nLCS Inflection and Loss of Hyperbolicity

Figure 3 displays the LCS evolution in the near wake without the rate-of-strain filter applied in rows one and three, and with the rate-of-strain filter applied in rows two and four. The images in figures 3–4 span one period of vortex shedding ( $T$ ) in steps of  $T/12$ . The image frame is centered on the top half of the wake

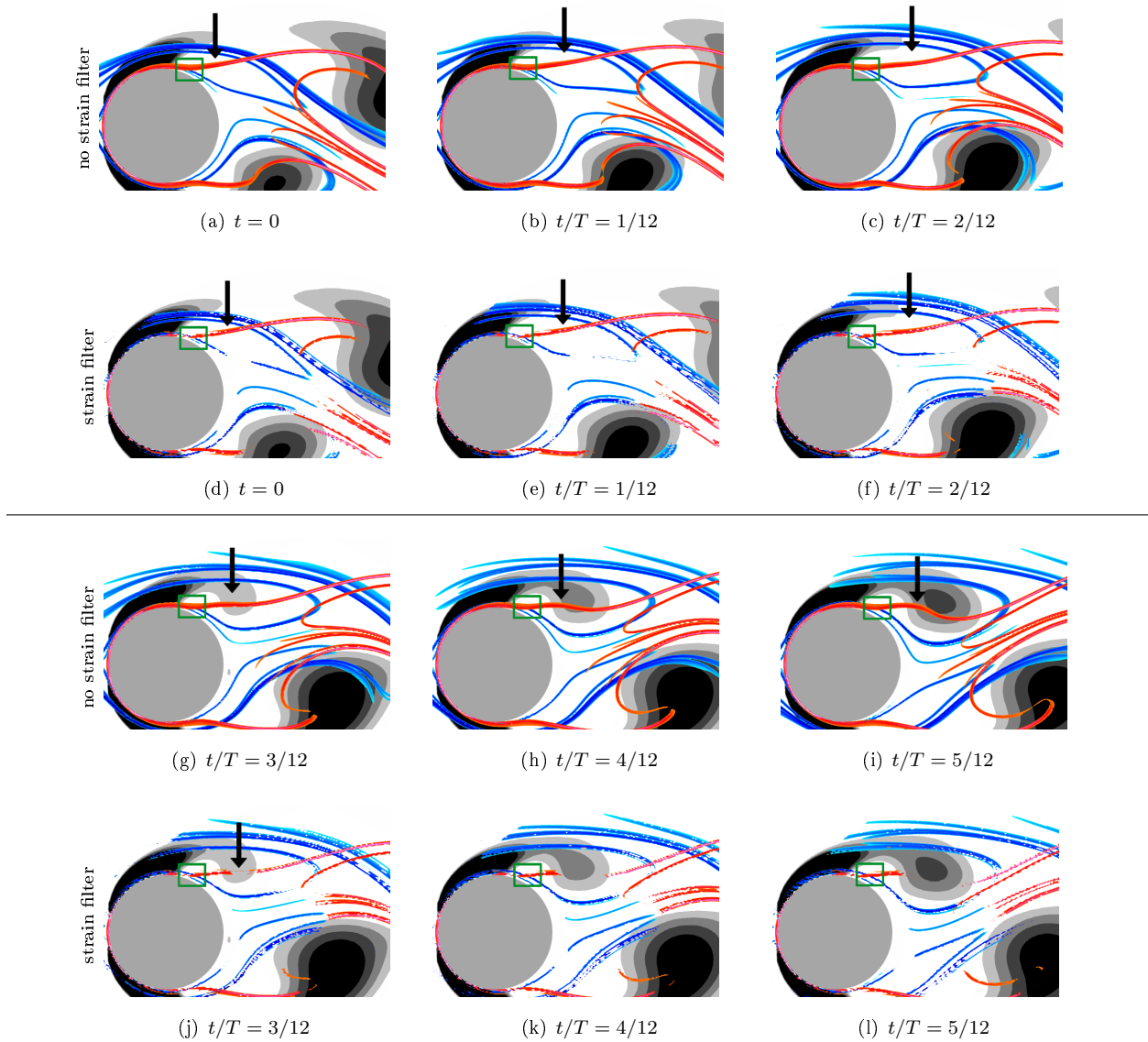


Figure 3. Vortex formation in near wake during first half of the shedding period shown by LCS and the  $Q$  criterion.

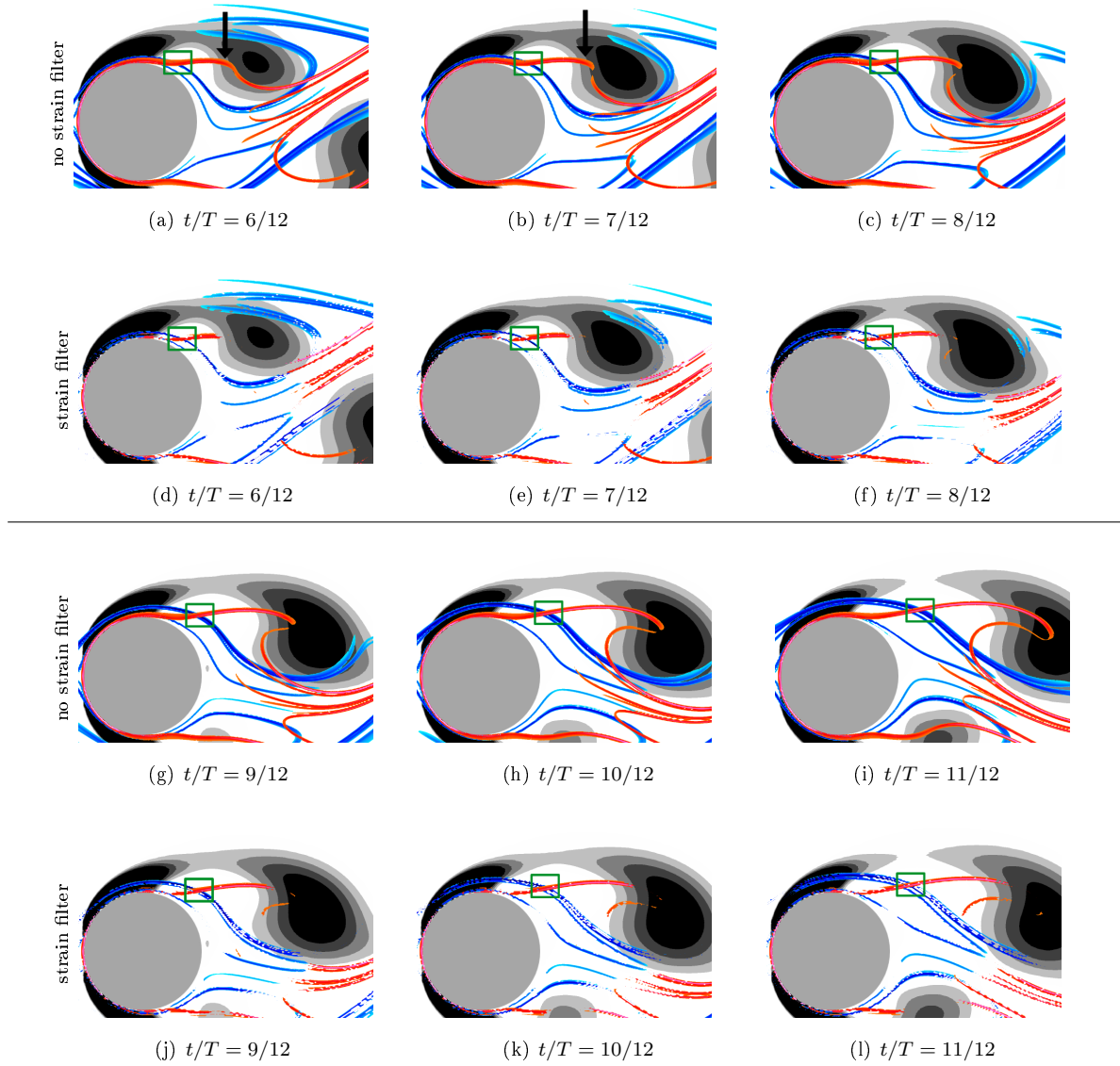


Figure 4. Vortex formation in near wake during second half of the shedding period shown by LCS and the  $Q$  criterion.

to focus on the formation of the single clockwise-rotating (CW) structure from the top side of the cylinder surface. The dark grey region (high  $Q$ ) exiting the field of view downstream of the cylinder in figure 3(a) is the vortex that was shed from the top of the cylinder in the previous period. The region of high  $Q$  at the bottom center of the figure 3(a) is the counter-clockwise (CCW) vortex that formed at the bottom of the cylinder in the previous half-period. The cylinder is indicated by the grey circular region in the left half of each frame, as neither LCS nor  $Q$  is detected in this region. The black arrow in figure 3(a) and each subsequent figure highlights the region along the top of the cylinder where the next CW vortex will form.

One thick and one thin pLCS (blue, repelling ridges) in figure 3(a) separate the near wake region from the vortex shed in the previous period. In figure 3(b), the thicker pLCS ridge breaks into two structures, and both begin to travel downstream with the shed vortex while the upstream, thin branch stays closer to the cylinder and begins to outline the region in which the next CW vortex will begin to form (highlighted by a black arrow). Meanwhile, an inflection point appears along the nLCS (red), begins to pinch up in figure 3(g), and then breaks apart and wraps around the newly forming vortex starting in figure 4(b) (also highlighted by the black arrow).

Also shown are the nLCS and pLCS filtered using equation 5. Of particular interest is the nLCS near the core of the developing vortex, in the time between figures 3(f) and 3(j). At earlier times, the nLCS extends from the cylinder surface intact. At the time the CW vortex begins to form (figure 3(j)), a clear break occurs along the nLCS (shown by a black arrow), which coincides with the emergence of positive  $Q$  criterion. This “breaking” of the nLCS depicts the loss of hyperbolic particle attraction along that segment of the nLCS ridge, and is even easier to identify than the change of nLCS curvature (inflection point). The gap along the ridge, indicating a loss of hyperbolic attraction, is necessary for the entrainment and rotation of fluid in this region.

In this particular simulation, the formation of the new CW vortex is observable at the same time and location with FTLE and with the  $Q$  criterion; a light grey region extending from the cylinder surface is clearly seen in the same region as the nLCS inflection point in figure 3(g). It is important to note, however, that in velocity data measured from experiments, an isosurface of 1%  $Q_{max}$  or 10%  $Q_{max}$  is more commonly used to avoid errors in vortex identification due to noise. The evolution of the pLCS and nLCS makes it possible to identify vortex formation from the data earlier in the time series than it is observable using  $Q$  in more general applications.

Experimental results at  $Re = 9000$  for a portion of the shedding period are shown in figure 5. The colorbar displayed in figure 5(b) is for the  $Q$  criterion, and is the same for each subfigure. All images display the LCS as FTLE values greater than 67% of the maximum FTLE value. A threshold of 1%  $Q_{max}$  was used to highlight the vortex cores, while removing some of the erroneous regions caused by noise in the

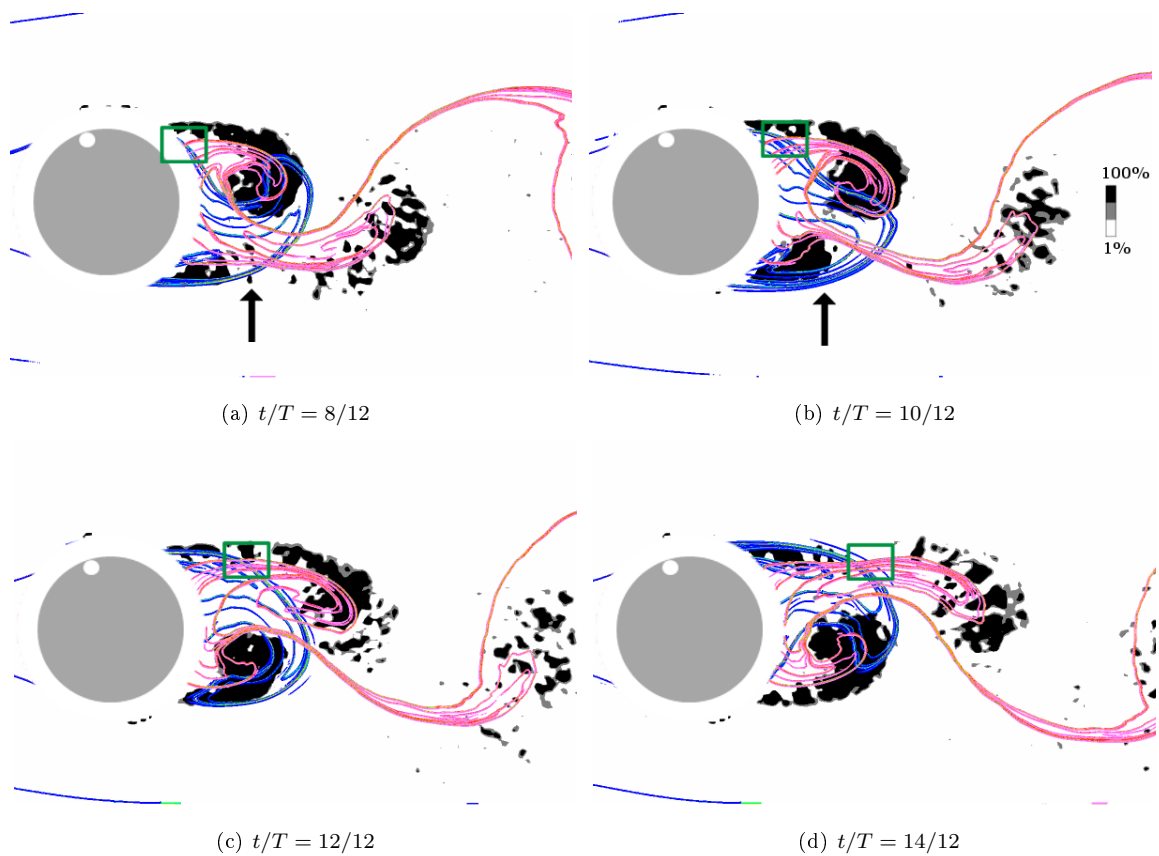


**Figure 5.** Experimental vortex formation at  $Re = 9000$  in the near wake shown by LCS (red, blue) and the  $Q$  criterion (greyscale).

experimental data. The white circle located inside of the grey cylinder is the location of the pressure tap used to measure the static pressure for phase averaging. The white ring surrounding the cylinder is the region obscured by the cylinder during the PIV experiments.

While the  $Q$  and FTLE results are not identical between the numerical and experimental data sets due to large differences in Reynolds number, the qualitative structure of the near-wake region of the flow is similar. Vortex cores highlighted by the  $Q$  criterion are shed in an alternating pattern from the top and bottom of the cylinder. The red nLCS wraps around the outside of the vortices while the blue pLCS separates the vortices from each other and the cylinder. The inflection point along the nLCS, indicative of a formation of the new vortex beginning, can be seen for the forming CCW structure on the bottom half of the cylinder wake between figures 5(a) and 5(b), and is indicated by the black arrow. The rate-of-of-strain filter is not effectively employed with the experimental data, because it necessitates taking the gradient of the noisier data field. For this reason, it is not included here.

## B. Vortex Shedding Identification via Saddle Point Tracking

Since the nLCS and pLCS are attracting and repelling lines in these two-dimensional examples, their intersections can be considered topological saddle points in the flow. Following the saddles associated with particular vortices has been shown to provide additional information about vortex wake evolution such as the locations of vortex boundaries and where vortex wake structures break down.<sup>24</sup> In the current work on vortex shedding from a cylinder, each newly forming vortex has an associated saddle point at the location where the nLCS we have discussed so far meets the cylinder surface, highlighted with a green box in figures 3–4. As time progresses, both the blue pLCS and the saddle point eventually lift off and detach from the cylinder surface and move with the fully formed CW vortex downstream. Notably, the observed saddle point dynamics are not affected by the rate-of-strain filter, proving that they are indeed structures in regions of hyperbolically attracting and repelling trajectories, and are dynamically robust against flow field perturbations that disrupt gradient-based methods, such as the  $Q$  criterion.

The location of the vortex center and the saddle point are tracked in space as shown in figures 6 and 7. The center of the vortex (red squares) is taken as the location with the maximum value of  $Q$ , and the saddle point location (blue triangles) is the center of the saddle point. The distance ( $d/D$ ) is measured to a stationary location on the cylinder surface, which was closest to the initial saddle point location, and is non-dimensionalized by the cylinder diameter. Figure 6 was generated using the same set of data used in figures 3–4.

When considering the saddle point distance traveled from the cylinder surface, it can be inferred that there are three different phases that make up the vortex shedding process. The first phase is during the vortex formation that occurs between 0 and approximately  $1/2$  of a period. In this time frame (corresponding to figure 3(a) to figure 3(i)) the vortex is forming behind the cylinder and the saddle point moves downstream only slightly as the vortex grows in size. In this phase of vortex shedding, the saddle point track is nearly horizontal as indicated by the solid black line in figure 6. The structure then separates from the cylinder between  $t/T = 5/12$  and  $t/T = 11/12$  (figure 4(a) to figure 4(i)). This is apparent in figure 6 as the saddle point accelerates away from the cylinder surface until reaching a constant velocity around  $t/T = 11/12$ , as indicated by the dashed line in figure 6. At this point, the vortex is separated completely from the cylinder surface, and both the vortex and the saddle point move downstream at a nearly constant convection speed that is roughly 60% of the free stream velocity.

In the track of the vortex core as identified by location of maximum  $Q$  value (red squares), there is no clear change in the core trajectory between the times when the vortex is forming, and when it sheds. There is a slight increase in downstream velocity (as indicated by increased slope in figure 6), but this change is gradual, and cannot be used to identify a shedding time.

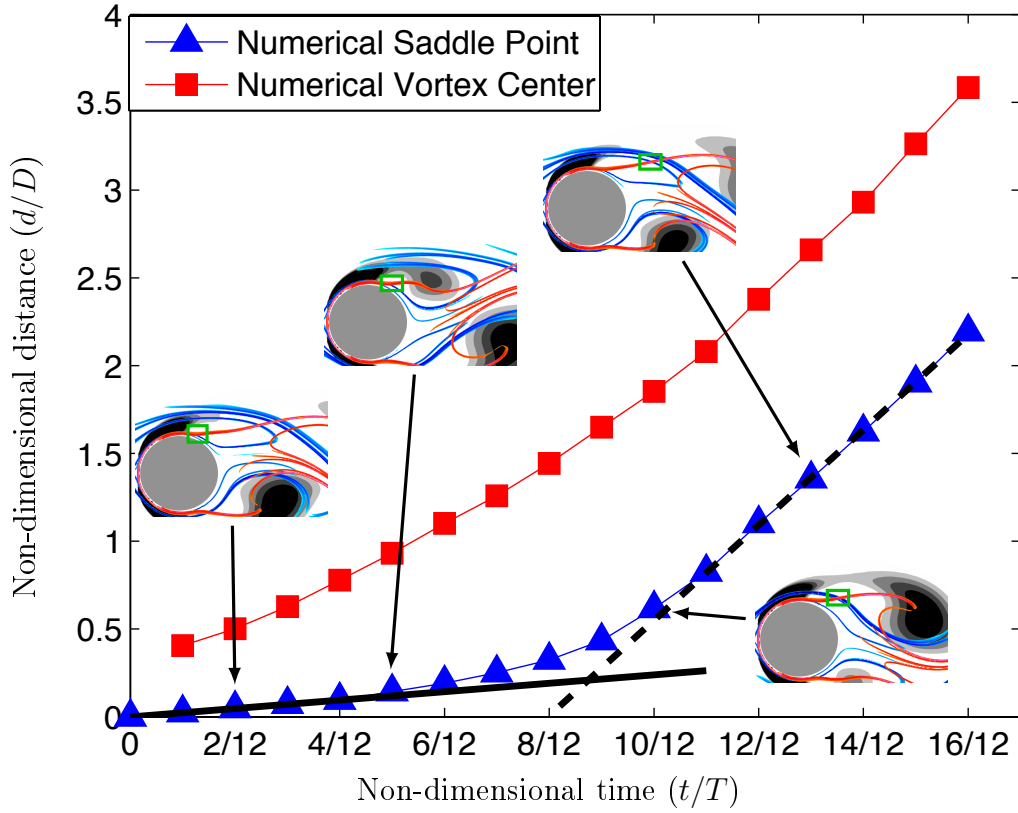


Figure 6. Saddle point distance and vortex distance from the cylinder surface in the numerical simulation. Corresponding snapshots of  $Q$  and FTLE are shown in inset, with their times indicated.

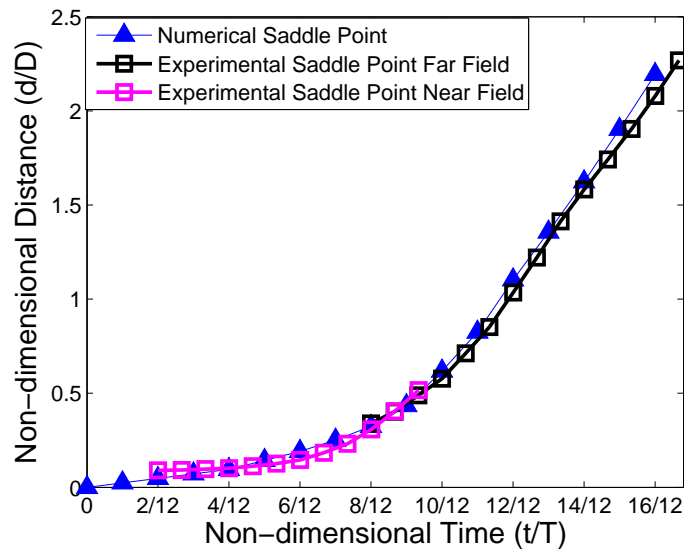


Figure 7. Saddle point distance and vortex distance from the cylinder surface including derived from both numerical ( $Re = 100$ ) and experimental ( $Re = 9000$ ) data.

Figure 7 displays the distance from the saddle point to the cylinder surface for both the numerical and experimental datasets. The timing of the numerical and experimental data sets were matched by visually comparing the scaled downstream wake organization. While there may be small errors associated with the precise timing match between the two data sets, the trajectories of the saddle points, highlighted by the green box in figure 5, is nearly identical. Any change in the phase would only result in a horizontal shift of the saddle point trajectory curve along the  $x$ -axis, not a change in the shape of the trajectory in time. The black squares in the figure correspond to the experimental data in figure 5, while the pink squares correspond to a small dataset that was collected specifically to resolve the near cylinder region. The experimental location of the saddle point is nearly identical to the numerical results when normalized by shedding period and cylinder diameter. The experimental results also show the same three phases of the vortex shedding process, and have a similar final convection speed of the vortex.

#### IV. Discussion and summary

Dynamics of both nLCS (attracting ridges) and pLCS (repelling ridges) in the region of new vortex core formation have been shown previously in the literature to provide information on the vortex structure of wakes. In the case of piston generated vortex rings,<sup>54</sup> it was observed that the separation of the pLCS was a precursor to the formation of another discrete vortex in the flow. In the work studying an isolated hairpin vortex in a fully three-dimensional turbulence DNS,<sup>24</sup> the pinch-up of nLCS is similar to that shown in the current work. In the hairpin vortex case the “breaking” of the nLCS shown by the strain filter also corresponded to the onset of fluid entrainment into newly forming vortex structures. Other work has used Lagrangian saddle points and their relation to vortices in a turbulent channel and behind a pitching panel,<sup>33</sup> on a pitching wing,<sup>35</sup> in ABC flow, and in the draft tube of a Francis water turbine.<sup>55</sup> The results presented here are novel in that we use saddle point tracking in related numerical and experimental data sets in order to demonstrate the robustness of the method, and its potential in a wide range of applications involving vortex formation and shedding due to fluid-structure interaction.

In the cylinder near wake, the upstream saddle point for each vortex is located on the cylinder surface while the structure is still forming. Once the saddle point (highlighted with the green box in figures 3–4) lifts off the cylinder surface, the vortex begins to move downstream from the cylinder and sheds around  $t = 5T/12$  (figure 3(i)). These saddle points are important since they are consistently observable components of the flow topology, robust to velocity field perturbations and noise inherent in experimental data. In the case considered here, using the point of maximum  $Q$  criterion to track the vortex core shows gradual motion away from the cylinder. This tracking method, which uses the flow field gradient, would not be reliable in more error-prone data sets **such as the experimental data presented.**

The methods used in the current analysis can be applied to a variety of flows and Reynolds numbers as long as the vortices induce distinct coherent motions in the flow that would be evident in the particle flow maps. The LCS would then still find transport barriers near the boundaries of the vortices, and the results should qualitatively be similar to the current results. One issue that may arise from a large increase in  $Re$  is an appropriate implementation of the method. Higher  $Re$  would create a separation of length- and time-scales of the coherent motions in the flow field, and a more careful approach regarding flow map integration time may be needed. If the vortex shedding can be associated with the dynamics of the large-scale structure, however, a similar implementation should produce similar results.

The current observations provide new insight to the fundamental understanding of vortex formation and shedding. The positive-time FTLE ridges indicate where flow will diverge by the integration time  $\tau$ . Therefore, regions around upstream saddle points could be candidates for further research in order to map the connection between the LCS dynamics with the observable quantities on the cylinder surface, such as pressure and velocity. This framework will have implications for unsteady flow modeling and flow control, exploring the possibility of dictating the behavior of the total flow field by focusing on the key topological points uncovered by the LCS analysis.

By incorporating an LCS analysis with well-established Eulerian vortex identification methods ( $Q$  criterion), we are able to establish new identification criteria for vortex roll up and shedding in the wake of a circular cylinder in cross-flow. The LCS analysis is more computationally intensive to calculate, but its phenomenological nature might lend it to schemes for identifying these physical events automatically from data with minimal user input and interpretation.

## V. Acknowledgements

The authors would like to thank Phillip Munday for his support with the numerical simulation. This work was supported by the Air Force Office of Scientific Research under Award No. FA9550-14-1-0210.

## References

<sup>1</sup>Williamson, C. and Roshko, A., "Vortex formation in the wake of an oscillating cylinder," *Journal of Fluids and Structures*, Vol. 2, No. 4, 1988, pp. 355 – 381.

<sup>2</sup>Baarholm, G., Larsen, C., and Lie, H., "On fatigue damage accumulation from in-line and cross-flow vortex-induced vibrations on risers," *Journal of Fluids and Structures*, Vol. 22, No. 1, 2006, pp. 109 – 127.

<sup>3</sup>Tognarelli, M., Taggart, S., and Campbell, M., "Actual VIV fatigue response of full scale drilling risers: with and without suppression devices," *Proceedings of the ASME 27th International Conference on Offshore Mechanics and Arctic Engineering*, 2008.

<sup>4</sup>Griffin, O. M., "A note on bluff body vortex formation," *Journal of Fluid Mechanics*, Vol. 284, 1 1995, pp. 217–224.

- <sup>5</sup>Gerrard, J. H., “The mechanics of the formation region of vortices behind bluff bodies,” *Journal of Fluid Mechanics*, Vol. 25, 5 1966, pp. 401–413.
- <sup>6</sup>Perry, A. E., Chong, M. S., and Lim, T. T., “The vortex-shedding process behind two-dimensional bluff bodies,” *Journal of Fluid Mechanics*, Vol. 116, 2 1982, pp. 77–90.
- <sup>7</sup>Triantafyllou, G. S., Triantafyllou, M. S., and Chryssostomidis, C., “On the formation of vortex streets behind stationary cylinders,” *Journal of Fluid Mechanics*, Vol. 170, 8 1986, pp. 461–477.
- <sup>8</sup>Strykowski, P. J. and Sreenivasan, K. R., “On the formation and suppression of vortex ‘shedding’ at low Reynolds numbers,” *Journal of Fluid Mechanics*, Vol. 218, 8 1990, pp. 71–107.
- <sup>9</sup>Boghosian, M. E. and Cassel, K. W., “A pressure-gradient mechanism for vortex shedding in constricted channels,” *Physics of Fluids*, Vol. 25, No. 12, 2013.
- <sup>10</sup>Tang, S. and Aubry, N., “On the symmetry breaking instability leading to vortex shedding,” *Physics of Fluids*, Vol. 9, No. 9, 1997, pp. 2550–2561.
- <sup>11</sup>Takemoto, Y. and Mizushima, J., “Mechanism of sustained oscillations in a fluid flowing past a circular cylinder obstacle,” *Phys. Rev. E*, Vol. 82, Nov 2010, pp. 056316.
- <sup>12</sup>Giannetti, F. and Luchini, P., “Structural sensitivity of the first instability of the cylinder wake,” *Journal of Fluid Mechanics*, Vol. 581, 6 2007, pp. 167–197.
- <sup>13</sup>Catalano, P., Wang, M., Iaccarino, G., Sbalzarini, I. F., and Kuomoutsakos, P., “Optimization of cylinder flow control via actuators with zero net mass flux,” *Center for Turbulence Research, Proceedings of the Summer Program*, 2002.
- <sup>14</sup>Artana, G., Sosa, R., Moreau, E., and Touchard, G., “Control of the near-wake flow around a circular cylinder with electrohydrodynamic actuators,” *Experiments in Fluids*, Vol. 35, 2003, pp. 580–588.
- <sup>15</sup>Lim, H.-C. and Lee, S.-J., “Flow control of a circular cylinder with O-rings,” *Fluid Dynamics Research*, Vol. 35, No. 2, 2004, pp. 107 – 122.
- <sup>16</sup>Lee, S.-J., Lim, H.-C., Han, M., and Lee, S. S., “Flow control of circular cylinder with a V-grooved micro-riblet film,” *Fluid Dynamics Research*, Vol. 37, No. 4, 2005, pp. 246 – 266.
- <sup>17</sup>Jukes, T. N. and Choi, K.-S., “Flow control around a circular cylinder using pulsed dielectric barrier discharge surface plasma,” *Physics of Fluids*, Vol. 21, No. 8, 2009, pp. 084103.
- <sup>18</sup>Dong, S., Triantafyllou, G. S., and Karniadakis, G. E., “Elimination of Vortex Streets in Bluff-Body Flows,” *Phys. Rev. Lett.*, Vol. 100, 2008, pp. 204501.
- <sup>19</sup>Perrin, R., Braza, M., Cid, E., Cazin, S., Moradei, F., Barthet, A., Sevrain, A., and Hoarau, Y., “Near-Wake Turbulence Properties in the High Reynolds Number Incompressible Flow Around a Circular Cylinder Measured by Two- and Three-Component PIV,” *Flow, Turbulence and Combustion*, Vol. 77, 2006, pp. 185–204, 10.1007/s10494-006-9043-5.
- <sup>20</sup>Braza, M., Perrin, R., and Hoarau, Y., “Turbulence properties in the cylinder wake at high Reynolds numbers,” *Journal of Fluids and Structures*, Vol. 22, No. 6–7, 2006, pp. 757 – 771.
- <sup>21</sup>Brown, G. L. and Roshko, A., “On density effects and large structure in turbulent mixing layers,” *Journal of Fluid Mechanics*, Vol. 64, 4 1974, pp. 775–816.
- <sup>22</sup>Hunt, J., Wray, A., and Moin, P., “Eddies, streams, and convergence zones in turbulent flows,” *Center for Turbulence Research, Proceedings of the Summer Program*, 1988.
- <sup>23</sup>Haller, G., “Distinguished material surfaces and coherent structures in three-dimensional fluid flows,” *Physica D*, Vol. 149, 2001, pp. 248–277.
- <sup>24</sup>Green, M., Rowley, C., and Haller, G., “Detection of Lagrangian coherent structures in three-dimensional turbulence,” *Journal of Fluid Mechanics*, Vol. 572, 2007, pp. 111–120.

- <sup>25</sup>Green, M., Rowley, C., and Smits, A., “The unsteady three-dimensional wake produced by a trapezoidal pitching panel,” *Journal of Fluid Mechanics*, Vol. 685, 2011, pp. 117–145.
- <sup>26</sup>O’Farrell, C. and Dabiri, J. O., “Pinch-off of non-axisymmetric vortex rings,” *Journal of Fluid Mechanics*, Vol. 740, 2014, pp. 61–96.
- <sup>27</sup>Beron-Vera, F., Olascoaga, M., and Goni, G., “Oceanic mesoscale eddies as revealed by Lagrangian coherent structures,” *Geophysical Research Letters*, Vol. 35, 2008.
- <sup>28</sup>Shadden, S. C. and Arzani, A., “Lagrangian postprocessing of computational hemodynamics,” *Annals of biomedical engineering*, Vol. 43, No. 1, 2015, pp. 41–58.
- <sup>29</sup>Eldredge, J. and Chong, K., “Fluid transport and coherent structures of translating and flapping wings,” *Chaos*, Vol. 20, 2010.
- <sup>30</sup>du Toit, P. and Marsden, J., “Horseshoes in hurricanes,” *Journal of Fixed Point Theory and Applications*, Vol. 7, 2010, pp. 351–384, 10.1007/s11784-010-0028-6.
- <sup>31</sup>Haller, G., “Lagrangian coherent structures,” *Annual Review of Fluid Mechanics*, Vol. 47, 2015, pp. 137–162.
- <sup>32</sup>Wang, Y., Haller, G., Banaszuk, A., and Tadmor, G., “Closed-loop Lagrangian separation control in a bluff body shear flow model,” *Physics of Fluids*, Vol. 15, No. 8, 2003, pp. 2251–2266.
- <sup>33</sup>Green, M., Rowley, C., and Smits, A., “Using hyperbolic Lagrangian coherent structures to investigate vortices in bio-inspired fluid flows,” *Chaos*, Vol. 20, 2010.
- <sup>34</sup>Huang, Y. and Green, M. A., “Eulerian and Lagrangian methods for detecting vortex formation and shedding,” *AIAA Science and Technology Forum*, 2015.
- <sup>35</sup>Mulleners, K. and Raffel, M., “The onset of dynamic stall revisited,” *Experiments in fluids*, Vol. 52, No. 3, 2012, pp. 779–793.
- <sup>36</sup>Chong, M., Perry, A., and Cantwell, B., “A general classification of three-dimensional flow fields,” *Physics of Fluids*, Vol. 2, 1990, pp. 765–777.
- <sup>37</sup>Jeong, J. and Hussein, F., “On the identification of a vortex,” *J. Fluid Mech.*, Vol. 285, 1995, pp. 69–94.
- <sup>38</sup>Graftieaux, L., Michard, M., and Grosjean, N., “Combining PIV, POD and vortex identification algorithms for the study of unsteady turbulent swirling flows,” *Measurement Science and Technology*, Vol. 12, No. 9, 2001, pp. 1422.
- <sup>39</sup>Haller, G. and Beron-Vera, F. J., “Geodesic theory of transport barriers in two-dimensional flows,” *Physica D: Nonlinear Phenomena*, Vol. 241, No. 20, 2012, pp. 1680 – 1702.
- <sup>40</sup>Brunton, S. L. and Rowley, C. W., “Fast computation of finite-time Lyapunov exponent fields for unsteady flows,” *Chaos: An Interdisciplinary Journal of Nonlinear Science*, Vol. 20, No. 1, 2010, pp. 017503.
- <sup>41</sup>Lipinski, D. and Mohseni, K., “A ridge tracking algorithm and error estimate for efficient computation of Lagrangian coherent structures,” *Chaos: An Interdisciplinary Journal of Nonlinear Science*, Vol. 20, No. 1, 2010.
- <sup>42</sup>Haller, G. and Sapsis, T., “Lagrangian coherent structures and the smallest finite-time Lyapunov exponent,” *Chaos*, Vol. 21, No. 023115, 2011.
- <sup>43</sup>Haller, G., “Lagrangian coherent structures from approximate velocity data,” *Physics of Fluids*, Vol. 14, No. 6, 2002, pp. 1851.
- <sup>44</sup>Olcay, A. B., Pottbaum, T. S., and Krueger, P. S., “Sensitivity of Lagrangian coherent structure identification to flow field resolution and random errors,” *Chaos: An Interdisciplinary Journal of Nonlinear Science*, Vol. 20, No. 1, 2010, pp. 017506.
- <sup>45</sup>Mathur, M., Haller, G., Peacock, T., Ruppert-Felsot, J. E., and Swinney, H. L., “Uncovering the Lagrangian skeleton of turbulence,” *Physical Review Letters*, Vol. 98, No. 14, 2007, pp. 144502.

<sup>46</sup>Olascoaga, M. J. and Haller, G., “Forecasting sudden changes in environmental pollution patterns,” *Proceedings of the National Academy of Sciences*, 2012.

<sup>47</sup>Taira, K. and Colonius, T., “The immersed boundary method: A projection approach,” *Journal of Computational Physics*, Vol. 225, No. 2, 2007, pp. 2118 – 2137.

<sup>48</sup>Colonius, T. and Taira, K., “A fast immersed boundary method using a nullspace approach and multi-domain far-field boundary conditions,” *Computer Methods in Applied Mechanics and Engineering*, Vol. 197, No. 25–28, 2008, pp. 2131 – 2146.

<sup>49</sup>Munday, P. M. and Taira, K., “On the lock-on of vortex shedding to oscillatory actuation around a circular cylinder,” *Physics of Fluids (1994-present)*, Vol. 25, No. 1, 2013.

<sup>50</sup>Kourentis, L. and Konstantinidis, E., “Uncovering large-scale coherent structures in natural and forced turbulent wakes by combining PIV, POD, and FTLE,” *Experiments in Fluids*, Vol. 52, No. 3, 2011, pp. 749–763.

<sup>51</sup>Bourgeois, J., Sattari, P., and Martinuzzi, R., “Coherent vortical and straining structures in the finite wall-mounted square cylinder wake,” *International Journal of Heat and Fluid Flow*, Vol. 35, 2012, pp. 130 – 140, 7th Symposium on Turbulence & Shear Flow Phenomena (TSFP7).

<sup>52</sup>Perrin, R., Braza, M., Cid, E., Cazin, S., Barthet, A., Sevrain, A., Mockett, C., and Thiele, F., “Obtaining phase averaged turbulence properties in the near wake of a circular cylinder at high Reynolds number using POD,” *Experiments in Fluids*, Vol. 43, No. 2-3, 2007, pp. 341–355.

<sup>53</sup>Rockwood, M. P., Loiselle, T., and Green, M. A., “Practical concerns of implementing an LCS analysis with underresolved data,” *Chaos*, Submitted.

<sup>54</sup>O’Farrell, C. and Dabiri, J. O., “A Lagrangian approach to identifying vortex pinch-off,” *Chaos*, Vol. 20, No. 017513, 2010.

<sup>55</sup>Sadlo, F. and Peikert, R., “Visualizing Lagrangian coherent structures and comparison to vector field topology,” *Topology-Based Methods in Visualization II*, Springer, 2009, pp. 15–29.